



Article

Composite Fault Diagnosis of Aviation Generator Based on EnFWA-DBN

Zhangang Yang ¹, Xingwang Bao ¹, Qingyu Zhou ¹ and Juan Yang ^{2,*}

¹ College of Electronic Information and Automation, Civil Aviation University of China, Tianjin 300300, China; yangcauc@163.com (Z.Y.); bao_xingwang@163.com (X.B.); 2022021075@cauc.edu.cn (Q.Z.)

² Engineering Techniques Training Center, Civil Aviation University of China, Tianjin 300300, China

* Correspondence: haishi_yj11@126.com

Abstract: Because of the existence of composite faults, which consist of both short-out and eccentricity faults, the characteristics of the output voltage and internal magnetic field of aviation generators are less different than those of single short-out faults; this causes the eccentricity fault to be difficult to identify. In order to solve this problem, this paper proposes a fault diagnosis method using an enhanced fireworks algorithm (EnFWA) to optimize a deep belief network (DBN). The aviation generator model is built according to the finite element method (FEM), whereas the output of different combinations of composite faults are obtained using simulations. The EnFWA algorithm is used to train and optimize the DBN network to obtain the best structure. Meanwhile, an extreme learning machine (ELM) classifier performs fault diagnosis and classification on the test data. The diagnosis results show that a pinpoint accuracy can be achieved using the proposed method in the diagnosis of composite faults in aviation generators.

Keywords: composite fault; enhanced fireworks algorithm; deep belief network; extreme learning machine



Citation: Yang, Z.; Bao, X.; Zhou, Q.; Yang, J. Composite Fault Diagnosis of Aviation Generator Based on EnFWA-DBN. *Processes* **2023**, *11*, 1577. <https://doi.org/10.3390/pr11051577>

Academic Editors: Dapeng Zhang, Qiangda Yang and Yuwen You

Received: 30 March 2023

Revised: 5 May 2023

Accepted: 10 May 2023

Published: 22 May 2023



Copyright: © 2023 by the authors. Licensee MDPI, Basel, Switzerland. This article is an open access article distributed under the terms and conditions of the Creative Commons Attribution (CC BY) license (<https://creativecommons.org/licenses/by/4.0/>).

1. Introduction

As the main power supply of the aviation power system, an aviation generator provides energy for various electrical equipment onboard and ensures a steady functioning of the power supply system. According to the IEEE Std 493-2007 standard [1] and the statistics of the Electric Power Research Institute, among all kinds of generator faults, 37% of faults are related to the stator, 41% are caused by bearing faults, 10% are caused by the rotor, and 12% are caused by other faults [2].

When rotor eccentricity occurs, it is considered static eccentricity when the rotor rotation center is not the geometric center of the stator but the rotation center is fixed; in contrast, it is considered dynamic eccentricity when the rotor rotation center is not the geometric center of the stator and the rotation center is changed. Typical internal faults of aviation generators are mainly divided into electrical faults, which are represented by a short-out of stator and rotor windings, and mechanical faults, which are represented by rotor eccentricity and composite faults [3]. Aiming at addressing the composite fault of winding short-out and rotor eccentricity at the same time, many scholars have carried out fault research in different fields. Under normal operation and rotor interturn short-out conditions, the electromagnetic torque is constant without a harmonic component. Meanwhile, the static eccentricity of the air gap causes the electromagnetic torque to produce three times frequency components, and the electromagnetic torque under the composite fault produces both two and three times frequency components. The trend of each frequency amplitude is only different when the degree of the short-out or the degree of eccentricity is aggravated. Different types of single faults will cause different changes in the harmonic frequency components of the electromagnetic waveform and magnetic density. Ref. [4] pointed out that the short-out fault between the turns of the stator has a great impact

on the magnetic field and electromagnetic force of the motor. The vibration displacement curve of each part of the motor is not a simple superposition of each single fault. However, the common dynamic eccentricity fault and the influence of the actual generator winding structure on the fault characteristics were not considered in the study [5]. In [6], an air gap magnetic field model of a generator was established using an air gap permeability method. Unbalanced forces that act on the rotor and that are caused by a variety of faults and rotor vibration characteristics under electromechanical composite fault were analyzed. Furthermore, the interturn short-out fault of the rotor winding was diagnosed using the amplitude and phase. To solve the problem of the complicated calculation of the air gap permeability, in [7], the influence of various fault variables on the magnitude and direction of the unbalanced magnetic pull of the rotor was analyzed under the dual factors of static and dynamic eccentricity and short-out between turns of the excitation winding. Ref. [8] analyzed the stator radial vibration characteristics of a turbo-generator under normal operation, an air gap static eccentricity fault, a stator interturn short-out fault and composite fault of air gap static eccentricity, and a stator interturn short-out fault. The influence of the fault parameters on the stator vibration characteristics was analyzed. The results show that the tendency of stator radial deformation and the amplitudes of two, four, and six times frequency will intensify with the increase in the level of the stator short-out or static eccentricity fault of the air gap. In [9], the degree of the short-out fault and the location of the short-out fault on the winding was studied under a composite fault. This study mainly includes the frequency component, amplitude, and vibration response of the winding to the electromagnetic force. In [10], the electromagnetic force and mechanical response of the end winding of the generator stator before and after two single faults and composite mechanical faults were studied in detail. The influence of the pole number of the generator on the frequency component of the electromagnetic force and the influence of coil position, eccentric angle, and eccentricity on the electromagnetic force amplitude were analyzed. The theoretical derivation of generator internal magnetic field fault characteristics depend on different generator fault air gap permeability and air gap magnetic potential; thus, the derivation is complicated due to the combinations of factors, such as the short-out degree, short-out position, and eccentricity. In [11], single faults and composite faults were comparatively studied from the perspective of spectrum characteristics based on the rotor line current and stator line voltage. The analysis results show that the presence of static eccentricity will lead to the same frequency characteristic in the stator line voltage as the inter-turn short-out fault of the rotor winding, which may lead to misdiagnosis. Ref. [12] took the stator and rotor core of a generator as the research object and analyzed the temperature characteristics of the stator and rotor core of a generator under different operating states. Ref. [13] also studied rotor loss and the variation of temperature under short-out and eccentricity faults. In [14], a Fourier transform was used to extract the frequency characteristics of the eccentric vibration acceleration, and the eccentric mass and eccentric radius were predicted using the k-nearest neighbor and decision tree algorithm techniques. In [15], a multi-scale, high-order, singular spectrum analysis was used to extract the singular spectrum entropy characteristics of vibration signals, and the rotor unbalance fault was diagnosed by combining the genetic algorithm and variable prediction model techniques.

The DBN shows good feature extraction and generalization ability when it has been applied for diagnosing motor, transformer, gear box, and other parts [16]. In these studies, DBN structures are basically defined by experience. Improper number of layers or nodes will lead to a longer training duration or insufficient training, which are common problems that exist in deep learning models. In order to reduce the influence of the subjectivity of network parameters on the diagnosis results, a particle swarm optimization (PSO) approach was proposed in [17] to optimize the DBN structure and realized a transient stability evaluation of the power system. It can also improve the fault diagnosis efficiency of rotating rectifier of aviation generator. In addition, PSO-DBN was also applied to the feature extraction of bearing and power system fault, prediction of power system load, and

many other fields [18]. On this basis, a quantum PSO algorithm was used in [19] to optimize the DBN learning rate and completed analog circuit fault diagnosis. The determination of DBN parameters by these algorithms enables DBN to extract effective fault features accurately when processing high-dimensional non-linear data.

Based on this, because of the requirement of reliability and the inadequacy of the research on the composite fault diagnosis of aviation generator, it is necessary to study and identify the composite fault of aviation generator precisely. Therefore, a model of three layers of DBN and a single layer of ELM optimized by EnFWA is proposed in this paper. In Section 2, an aviation generator and a field-circuit coupling model are built by FEM to simulate the composite fault of short-out and eccentricity of the aviation generator with a multi-parallel branch structure. In Section 3, the structure of DBN-ELM and improvement of FWA are introduced. In addition, there are several combinations of other algorithms and models to compare with. In Section 4, fault data and labels of different faults used to train the model are listed. Furthermore, feature extraction and diagnosis of the faults are carried out. Then, both the result of training set and test set are shown to validate the proposed model. Finally, a brief conclusion is drawn to summarize the contribution of this paper in Section 5.

2. Aviation Generator Model

2.1. Aviation Generator Parameters

Rotor of aviation generator usually adopts salient pole structure. In addition to direct current (DC) field windings, there are damping windings on rotor core which can effectively improve the output quality. The inner surface of the stator core is uniformly slotted and embedded into the armature. The aviation generator designed in this paper needs to meet the rated capacity of 65 kVA, the rated voltage of 407 V, the rated speed of 8000 rpm, and frequency of 400 Hz. The main parameters of the generator to be calculated include the pole-pairs number p , stator slots number Z , stator slot area S , stator outer diameter D_s , rotor outer diameter D_r , gap length d_r , core length l_{ef} , etc. According to the principle of generator design, the larger the electromagnetic load A and B_δ are, the smaller the volume will be. The outer diameter of the stator and the length of the core can be roughly determined by l_{ef}/D_s , as shown in Equation (1):

$$D_s^2 l_{ef} = \frac{6.1 P_{em}}{\alpha_0 k_{wm} k_{dp} B_\delta A n_s} \quad (1)$$

where P_{em} is the rated power, n_s is the rated speed, α_0 is polar arc coefficient, k_{wm} is magnetic density waveform coefficient, and k_{dp} is winding coefficient.

According to Equation (2), the number of slots q for each pole can be determined. Then, the number of parallel branches a , current density J , and standard wire gauge can be used to determine the number of conductors and the diameter of the wire d_ϕ can be expressed as Equation (3):

$$q = \frac{Z}{2pm} \quad (2)$$

$$d_\phi = \sqrt{\frac{4I_N}{aJ\pi}} \quad (3)$$

where $m = 3$ is the number of phases and I_N is the rated current.

According to preliminary calculation and fine-tuning, main parameters of the generator are shown in Table 1.

2.2. FEM Model of the Aviation Generator

FEM is a numerical technique for obtaining the approximate solutions of partial differential equations. When solving the problem, the whole region is divided into several small regions and each part of the region becomes simple. The general process of FEM is model

creation, condition setting, meshing, and solving. FEM is widely used in electromagnetic simulation, fluid analysis, and many other fields [20].

Table 1. Main parameters of the generator.

Stator		Rotor	
Outer diameter/mm	230	Outer diameter/mm	158
inner diameter/mm	160	shaft diameter/mm	53.2
the number of slot	54	core length/mm	103
core length/mm	103	pole pairs	3
material	DW315_50	material	M27_24G
connection of winding	Y	turns each pole	50
winding pitch	6	width of pole shoe/mm	58.6
branch	2	height of pole shoe/mm	9.6
conductors per slot	10	pole-core width/mm	22
width of air gap/mm	1	pole-core height/mm	24
wire size/mm	1.219	polar arc coefficient	0.72
resistance of each phase/ Ω	0.126	resistance of field winding/ Ω	0.44

According to the parameters of the aviation generator in Table 1, the model is created by FEM and its structure is shown in Figure 1.

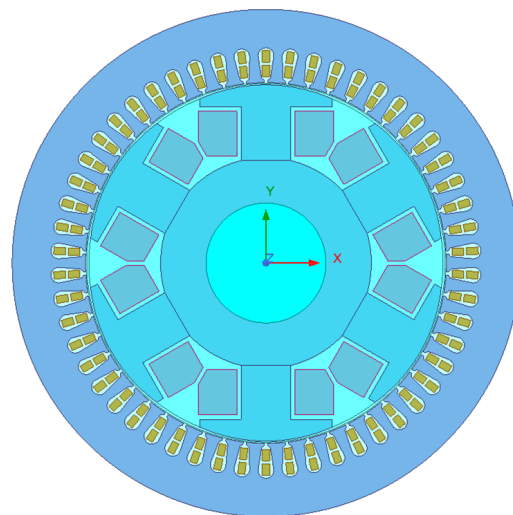


Figure 1. Finite element model.

There is power loss in the actual operation, mainly involving copper loss, hysteresis loss, eddy loss, friction, and wind loss. Among them, friction and wind loss are only related to rotational speed. In simulation, the rotational speed is constant and the friction and wind loss is about 300 W. Other losses can be calculated through simulation. While the field current is 18.6 A, the amplitude of no-load back electromotive force (BEF) is 332.84 V and its RMS value is about 235 V. Total harmonic contents of the BEF is 2.6%, as shown in Figure 2. Meanwhile, the magnetic field, which is shown in Figure 3, is not saturated. The no-load characteristic of the aviation generator is obtained. Under this condition, the generator works near the turning point of the magnetic saturation as shown in Figure 4.

The field-circuit coupling method is adopted to build the three-phase six-branch external load circuit, as shown in Figure 5, which can realize the load operation of the generator. Here, L_{phase} represents each branch winding, R is the equivalent resistance of each branch winding, and L is the leakage inductance. R_{load} and L_{load} are the load resistance and inductance of each phase, respectively.

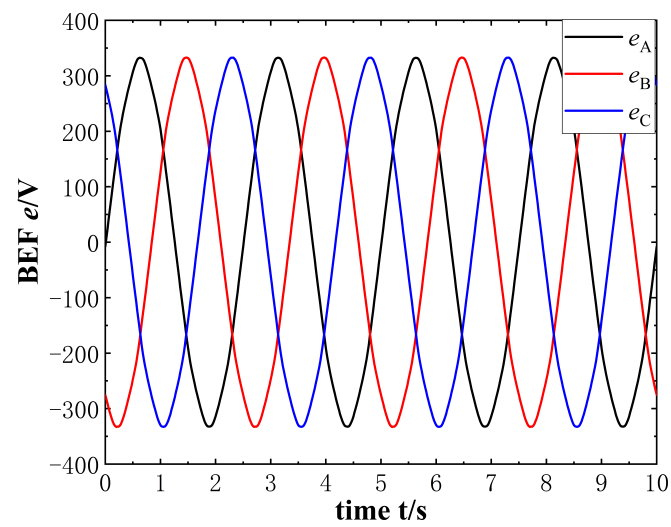


Figure 2. No-load BEF.

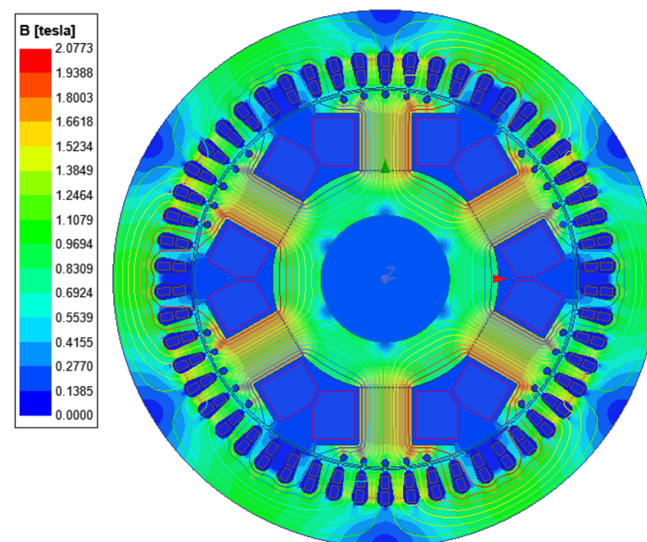


Figure 3. Magnetic density.

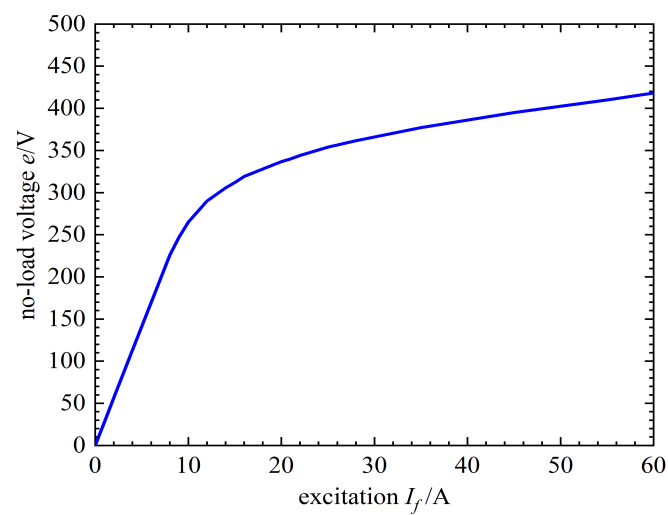


Figure 4. No-load characteristic.

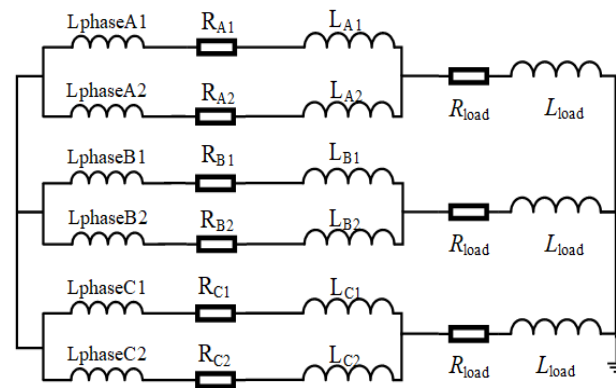


Figure 5. External circuit.

The equivalent leakage inductance $L = 0.112$ mH and the equivalent resistance $R = 0.126$ Ω at the end of each branch of the three-phase windings can be calculated by finite element simulation. According to the rated output, R_{load} and L_{load} of the external load circuit can be calculated as shown in Equation (4):

$$\begin{cases} Z_{load} = \sqrt{R_{load}^2 + (\omega L_{load})^2} \\ \tan\varphi = \frac{\omega L_{load}}{R_{load}} \end{cases} \quad (4)$$

When the generator runs with resistive load with the resistance value $R_{load} = 2.67$ Ω and the field current $I_f = 36$ A, the generator is operating under rated conditions. The amplitude of the output voltage is 332.481 V and its RMS value is 235.1 V. While the peak value of output current is 124.525 A and its RMS value is 88.04 A. The efficiency of the generator reaches 95.4%. As damping windings can inhibit distortion, the waveform of the output voltage and current of the generator is close to sine wave as shown in Figure 6. Because the winding pitch of the generator is $y = 2/3$, the effect of suppressing the triple harmonics can be achieved. In addition, affected by the harmonic magnetomotive force, the phase current mainly contains $6n \pm 1$ ($n = 0, 1, 2, \dots$) harmonic components. So the harmonic components of the phase current are mainly 5 and 7 times.

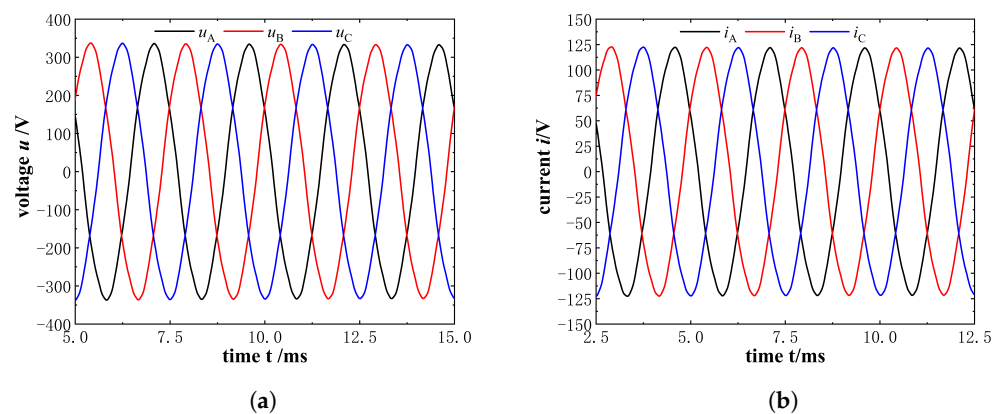


Figure 6. Rated output with resistive load: (a) Voltage. (b) Current.

2.3. Model of Composite Faults

The field-circuit coupling method, considering relative spatial position of short-out windings, separating out the short-out part from other windings and changing the resistance according to the degree of short-out in the corresponding coupling circuit, can be used to simulate the short-out fault, as shown in Figure 7. The simulation model for eccentricity is also shown in Figure 8. As shown in the figure, the gap length on both sides of the rotor is different.

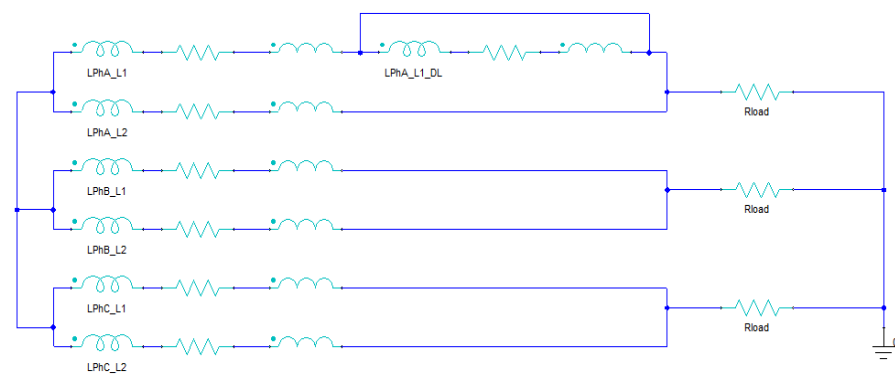


Figure 7. External circuit with short-out fault.

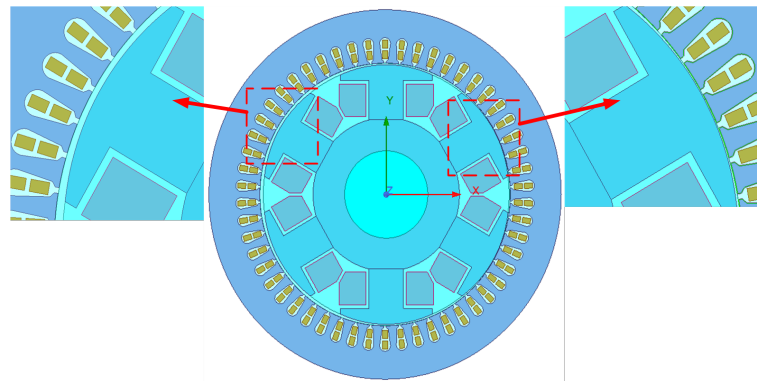


Figure 8. Simulation model of eccentricity.

In simulation, the eccentric direction is set as the positive direction of the X-axis. In the case of static eccentricity, the center of rotation and the geometric center of the rotor coincide with the X-axis. In the case of dynamic eccentricity, only the coordinate offset of the rotation center is set.

When the $LPhA_L1$ branch, which is shown in Figure 7, has 1/9 short-out, the leakage inductance of the branch winding L and the resistance R will be 0.0996 mH and 0.112 Ω . As the A-phase effective windings decreases, the amplitude of the A-phase current will also decrease. In order to balance the three-phase power and keep the terminal voltage constant, the current amplitude of other two phases will increase resulting in three-phase imbalance. Since the load carried by the generator is resistive, the distortion of the output voltage and current are basically the same with only different amplitudes as shown in Figure 9. The short-out between turns of the stator windings changes the distribution of magnetic density. Taking 1/9 short-out of the $LPhA_L1$ branch as an example, the positive part of magnetic density is severely distorted while the negative part is basically unchanged as shown in Figure 10.

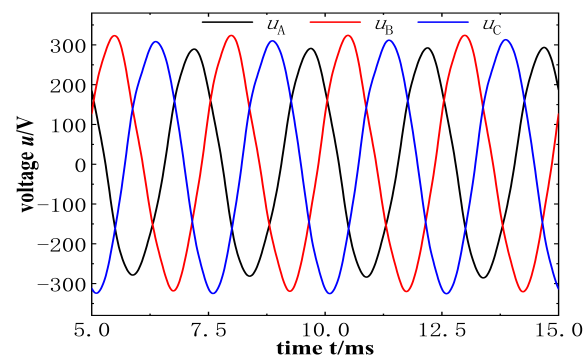


Figure 9. Output voltage under short-out.

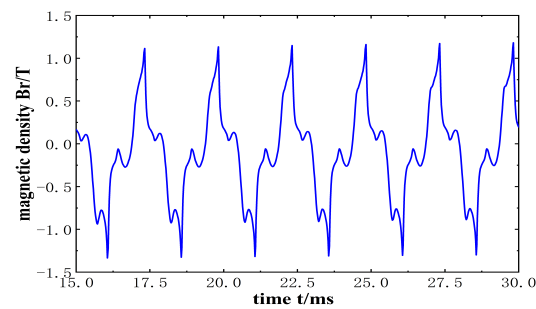


Figure 10. Magnetic density under short-out.

The time-domain waveform and the frequency components of magnetic density under static eccentricity at rated load operation are shown in Figure 11. As can be seen in the figure, the amplitude of each frequency component is increased with the degree of static eccentricity. Therefore, the time-domain waveform of magnetic density will be distorted due to static eccentricity.

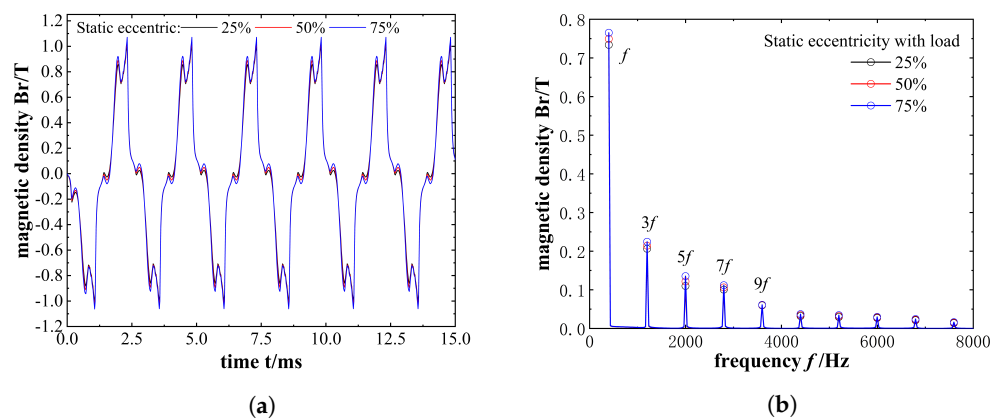


Figure 11. Magnetic density under static eccentricity: (a) Time-domain. (b) Frequency-domain.

The time-domain waveform and the frequency components of magnetic density under dynamic eccentricity at rated load are shown in Figure 12. The trend of magnetic density is the same as no-load condition and the frequency is newly added with harmonics, such as 533.3 Hz, 1066.7 Hz, and 1333.3 Hz. The distortion of the time-domain waveform of magnetic density is aggravated compared with the static eccentricity. Namely, dynamic eccentricity will do more damage to the stable operation of the generator and the reliability of aircraft power supply system.

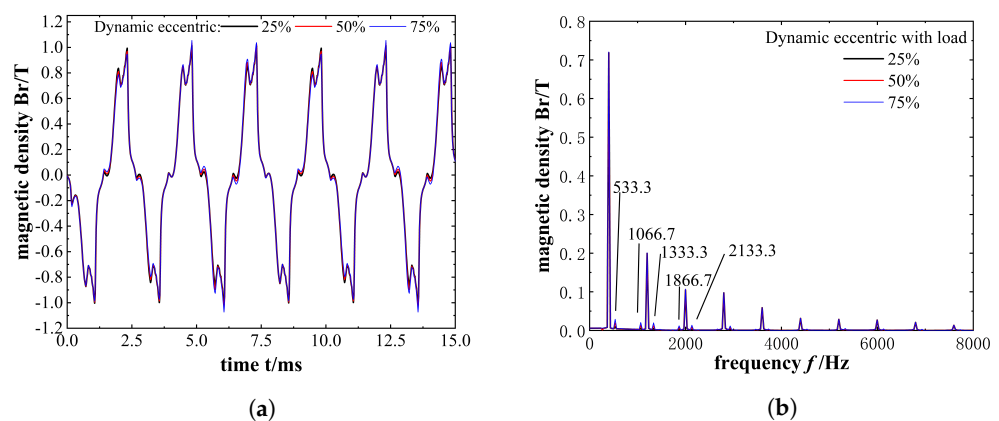


Figure 12. Magnetic density under dynamic eccentricity: (a) Time-domain. (b) Frequency-domain.

As the stator windings of the generator adopt $a = 2$ parallel branch structure, the two branches are located near and far from the eccentric position in space, respectively. So

the amplitude of the BEF on these two branches of each phase is different. The unbalance phenomenon of the BEF on these two branches will be offset by parallel branches. The amplitude of the BEF at the parallel output terminal does not change significantly in several electrical cycles. When the degree of static eccentricity is 25%, 50% and 75%, the output voltage of the A-phase parallel terminal at rated load is shown in Figure 13. When the generator is running at rated load, the output voltage of the parallel terminal increases because of the static eccentricity. Moreover, due to the influence of the armature reaction, the fractional harmonics, and the load type, the difference of the output of different fault degrees is more obvious than that under no-load conditions. In the case of dynamic eccentricity, the BEF of each branch is superimposed through the parallel structure and the amplitude of the A-phase BEF does not change significantly within several electrical cycles, as shown in Figure 14. However, it should be pointed out that the difference between the BEF of static eccentricity and dynamic eccentricity is imperceptible, which makes it difficult to distinguish and carry on the fault diagnosis.

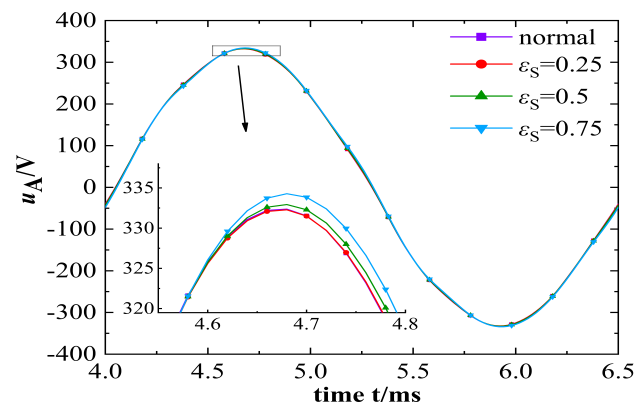


Figure 13. Output voltage under different degrees of static eccentricity.

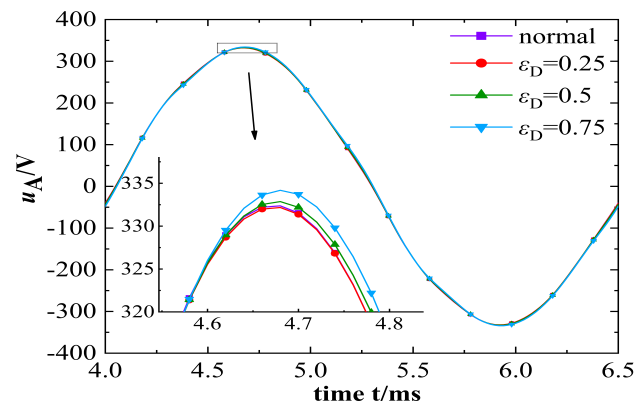


Figure 14. Output voltage under different degrees of dynamic eccentricity.

The three-phase output voltage and magnetic density under 25% dynamic eccentricity and 1/3 A-phase short-out are shown in Figure 15. The output voltage mainly reflects the characteristics of short-out. So it is not significantly different from the mere short-out. On the basis of short-out, the time-domain waveform of magnetic density adds the harmonics produced by dynamic eccentricity, that is, the magnetic density amplitude decreases periodically when $t = 17.5$ ms and 25 ms in Figure 15b.

When the characteristic of the composite fault is similar to the short-out the output characteristics are difficult to reveal the eccentricity. In addition, it can hardly distinguish whether the short-out fault caused the rotor eccentricity or the eccentricity occurred before the short-out. Therefore, the feature extraction and diagnosis of the composite fault are carried out in the next section.

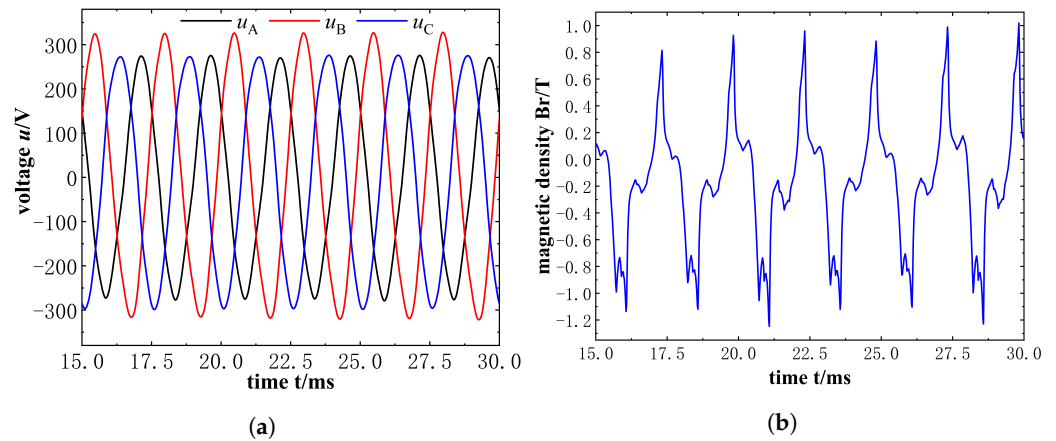


Figure 15. The 1/3 short-out and 25% dynamic eccentricity: (a) Output voltage. (b) Magnetic density.

3. Feature Extraction and Fault Diagnosis Algorithm

3.1. DBN

DBN consists of several restricted Boltzmann machines (RBM) which can be applied to feature learning, dimension reduction, and classification. Each layer of RBM is trained by unsupervised training method. The original features of input data are extracted gradually in the pre-training stage and the result will be used as initial value of the supervised training probability model with the gradient-based algorithm for reverse parameter adjustment. Advantages of supervised training and unsupervised training are combined to improve the learning performance. Figure 16 shows the structure of DBN.

The single RBM shown in Figure 17 is a probabilistic model consisting of visible layer and hidden layer. Only neurons between different layers are connected through weight vector w and bias vectors b and c .

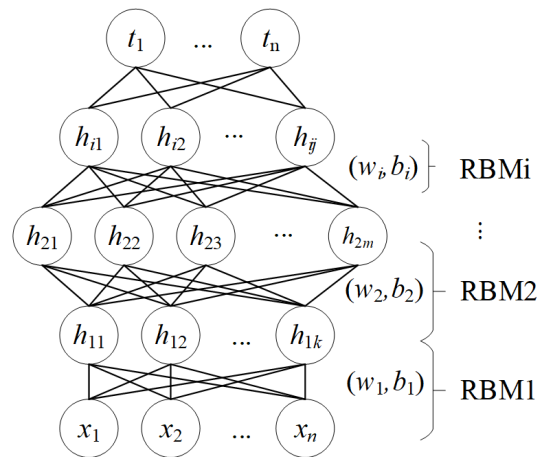


Figure 16. Structure of DBN.

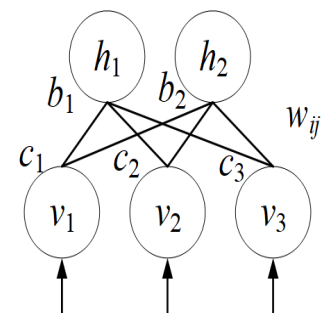


Figure 17. Structure of RBM.

The function between neurons of two layers is shown in Equation (5):

$$E(v, h) = - \sum_{i=1}^V \sum_{j=1}^H w_{ij} v_i h_j - \sum_{i=1}^V c_i v_i - \sum_{j=1}^H b_j h_j \quad (5)$$

where v_i and h_j are the input and output of each neurons in the two layers, respectively. w_{ij} is the weight of each layer. c_i and b_j are the bias vectors of two layers, respectively. V and H are the number of neurons.

The joint probability distribution between the two layers is shown in Equation (6):

$$P(v, h) = \frac{e^{-E(v, h)}}{\sum_v \sum_h e^{-E(v, h)}} \quad (6)$$

The conditional probability distribution of hidden layer vector h and visible layer vector v can be expressed by activation probability. Equation (7) represents the forward training process and Equation (8) represents the reverse reconstruction process.

$$P(h_j = 1|v) = \delta(b_j + \sum_i w_{ij} v_i) \quad (7)$$

$$P(v_i = 1|h) = \delta(c_i + \sum_j w_{ij} h_j) \quad (8)$$

The output of the single RBM is a binary variable of 0 or 1, the activation function adopts Sigmoid as shown in Equation (9):

$$\delta(t) = \frac{1}{1 + \exp(-t)} \quad (9)$$

In the training process, derivative of the log-likelihood function of the visible layer is shown in Equation (10):

$$\frac{\partial \log P(v, \theta)}{\partial \theta_{ij}} = (v_i h_j)_{data} - (v_i h_j)_{model} \quad (10)$$

where $\theta = \{w, b, c\}$, $(\)_{data}$ and $(\)_{model}$ is the mathematical expectation of $P(h|v)$ and $P(v|h)$, respectively.

RBM training adopts the contrastive divergence method to solve the error of the mathematical expectation of the reconstructed data by the gradient-based method until it reaches the maximum of the iteration. The parameter update method is shown in Equation (11):

$$\begin{cases} w_{ij}^{(n+1)} = w_{ij}^{(n)} + \eta [(v_i h_j)_o - (v_i h_j)_k] \\ b_j^{(n+1)} = b_j^{(n)} + \eta [(h_j)_o - (h_j)_k] \\ c_i^{(n+1)} = c_i^{(n)} + \eta [(v_i)_o - (v_i)_k] \end{cases} \quad (11)$$

where η is the learning rate and n is the number of iterations.

After the pre-training, θ is reversely fine-tuned to reduce the error E which is defined as Equation (12):

$$E(\theta) = \frac{1}{M} \sum_{m=1}^M (||t_m - y_m||^2) \quad (12)$$

where t_m is the label of input data and y_m is the output of pre-training.

As the number of iterations is constantly updated, the updating method is shown in Equation (13):

$$\theta = \theta - \eta \frac{\partial E(\theta)}{\partial \theta} \quad (13)$$

3.2. ELM

As can be seen from Figure 16, DBN network consists of the input layer, multiple RBMs, and classifiers that constitute the $[X-H_1-H_2-\dots-H_i-T]$ structure. In this paper, the extreme learning machine (ELM) is used as the classifier of label layer. The ELM different from the gradient-based method mainly features the random set of parameters of hidden layer nodes and the only calculation of the output weight. Non-linearity is introduced into the system because of the non-linear activation function in the hidden layer. Therefore, the convergence of ELM is faster than the traditional algorithm. At the same time, random hidden nodes guarantee the global approximation ability.

During training of ELM, different pairs of input and output (x_i, t_i) are required. Where $x_i = [x_{i1}, x_{i2}, \dots, x_{in}]^T \in R^n$, $t_i = [t_{i1}, t_{i2}, \dots, t_{im}]^T \in R^m$. The ELM model with the number of hidden layer nodes L can be expressed as Equation (14):

$$\sum_{i=1}^L \beta_i h(\omega_i \cdot x_j + b_i) = O_j \quad (14)$$

where $h(x)$ is the activation function of the hidden layer that provides non-linearity for the system. $\omega_i = [\omega_{i1}, \omega_{i2}, \dots, \omega_{in}]^T$ is the input weight matrix. β_i is the output weight matrix. b_i is the hidden layer bias. O_j is the output of the model.

The purpose of ELM training is to minimize the error, which is shown in Equation (15):

$$\sum_{j=1}^N ||O_j - t_j|| = 0 \quad (15)$$

The target matrix T can be expressed as Equation (16):

$$H\beta = T \quad (16)$$

$$H = \begin{bmatrix} h(\omega_1 \cdot x_1 + b_1) & \cdots & h(\omega_L \cdot x_L + b_L) \\ \vdots & \ddots & \vdots \\ h(\omega_1 \cdot x_N + b_1) & \cdots & h(\omega_L \cdot x_N + b_L) \end{bmatrix}_{N \times L} \quad (17)$$

where H is the output of hidden layer nodes. β is the output weight matrix. T is the target matrix.

In the course of the traditional gradient-based training, all parameters of the network are adjusted generally. While ELM only needs to determine the input weight of random variable ω_i and the hidden layer bias b_i . On this basis, through the model, the output matrix of hidden layer and the output weight β can be calculated. Therefore, the learning process of ELM network is essentially a system of linear equations solving. Equations are shown as Equation (18):

$$\beta' = H^+ T \quad (18)$$

where H^+ is the Moore–Penrose generalized inverse matrix of H .

To sum up, the feature extraction and the diagnostic performance of DBN-ELM is directly affected by the network learning ability which depends on the number of RBM layers and nodes. In order to avoid the influence of inappropriate parameters of the network on the training speed and accuracy of feature extraction, EnFWA will be introduced to obtain the optimal network structure and improve the feature extraction performance and diagnostic accuracy of the network.

3.3. EnFWA

Traditional fireworks algorithm has the disadvantages of inferior fitness and large search radius in the early stage. While the fitness improves, its searching radius decays quickly which is easy to fall into the local optimum and loses the general searching ability.

Fireworks with optimal fitness are kept when determining the next generation of fireworks, which can accelerate the decay of searching radius. In addition, fireworks for Gaussian mutation operation are randomly selected and the fitness value of these fireworks has a direct impact on the optimization, which leads to the error of the optimal solution. Existing research generally improve the algorithm from the perspective of explosion radius and quantity, fireworks mutation, and the next generation selection strategy in order to solve the local optimum of traditional FWA.

For the sake of coordinating the early general searching ability with the local searching ability in the later stage, dynamic adjustment factor and dynamic radius factor are introduced. The product of these two dynamic factors can realize the change of the explosion radius R_i dynamically with search update. The dynamic adjustment factor q and the dynamic radius factor μ_r are defined as Equations (19) and (20):

$$q = \left(1 - \frac{n}{N}\right)^\zeta \tag{19}$$

$$\mu_r = R_i \frac{f(x) - f_{min}}{f_{max} - f_{min}} \cdot \frac{n}{N} \tag{20}$$

In the formula, n is the number of current iterations. N is the maximum iteration. ζ is the adjustment coefficient. $f(x)$ is the fitness function of the error. f_{max} and f_{min} are the extreme values of the function.

In the later stage of the search, in order to avoid the explosion radius close to 0, the minimum explosion radius R_{min} is introduced to ensure the local search ability. The dynamic explosion radius is expressed as Equation (21):

$$R'_i = R_{min} + \left(1 - \frac{n}{N}\right)^\zeta \cdot R_i \frac{f(x) - f_{min}}{f_{max} - f_{min}} \cdot \frac{n}{N} \tag{21}$$

When the explosion radius is less than R_{min} , it will be taken as R_{min} . In each iteration, R'_{min} can be calculated according to the maximum and minimum radius in the previous iteration as shown in Equation (22),

$$R'_{min}(N) = q \cdot [R_{max}(n - 1) - R_{min}(n - 1)] \tag{22}$$

where t_i is introduced to simulate the falling of the actual fireworks explosion and the effect of it is defined as $e^{0.5gt_i^2}$. Here, $g = 9.8$ is the gravitational acceleration and the function is shown as Equation (23),

$$\begin{cases} x_{ij}^k = x_i^k + rand_1 \cdot R'_i - e^{0.5gt_i^2} \\ t_i = R_i / R_{max} \end{cases} \tag{23}$$

where R_{max} is the initial maximum explosion radius.

Since the roulette strategy is used to select the next generation of fireworks, $R(x_i)$ is the sum of mahalanobis distance between the current individual and other individuals. For a vector $x = (x_1, x_2, x_3, \dots, x_p)^T$ with mean value $\mu = (\mu_1, \mu_2, \mu_3, \dots, \mu_p)^T$ and covariance matrix S , the mahalanobis distance $R_M(x)$ can be expressed as Equation (24):

$$R_M(x) = \sqrt{(x - \mu)^T S^{-1} (x - \mu)} \tag{24}$$

Then, the probability $p(x_i)$ of each individual firework being selected is shown in Equation (25):

$$p(x_i) = \frac{R_M(x_i)}{\sum_{j \in k} R_M(x_j)} \tag{25}$$

In conclusion, the process of EnFWA is shown in Figure 18.

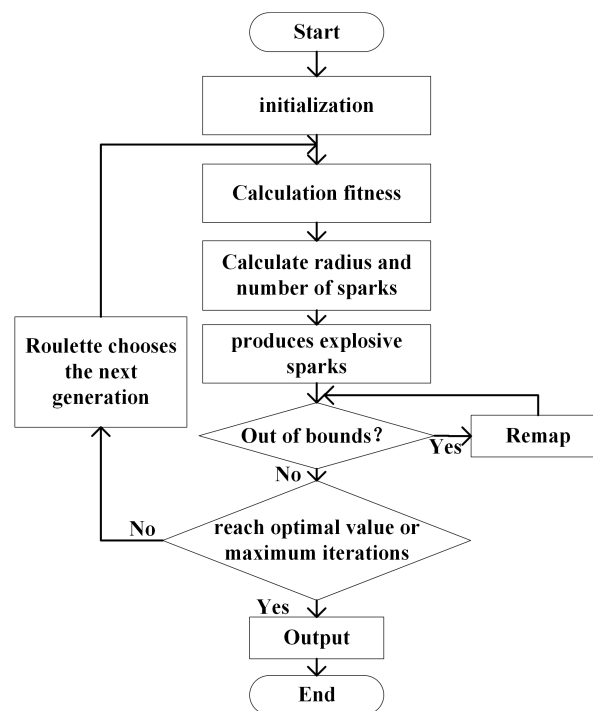


Figure 18. Process of EnFWA.

3.4. Comparisons of Different Diagnostic Models

In order to further verify the feature extraction and the diagnosis ability of EnFWA-DBN-ELM, different diagnostic models are used to identify the eccentricity fault and the composite fault. The following models are used in this section:

- (1) FFT + EnFWA + DBN: Preliminary feature extraction was carried out on the output voltage and current data with fast Fourier transform (FFT). Features of the first 20 frequency components were used for training and diagnosing with the same network structure.
- (2) PSO + DBN: PSO algorithm was used to train and optimize the DBN. The number of particles is 50, the acceleration coefficient $c_1 = c_2 = 0.5$, and the inertia weight decreased from 0.9 to 0.4.
- (3) SDAE + SVM: the stacked denoising autoencoder (SDAE) was used for feature extraction of the fault data and support vector machine (SVM) was used for fault diagnosis. The structure of SDAE hidden layer is [150–75–20], sparse coefficient is 0.15, penalty weight is 3, SVM penalty parameter $C = 49.43$, and kernel parameter $g = 100$.
- (4) LSTM + Softmax: The long short-term memory (LSTM) was used to extract fault data features and the softmax was used for fault diagnosis. Set the number of LSTM hidden layer neurons as [14–14], the learning rate as 0.01, and the length of sliding window as 10.

According to the above models and parameter settings, the training and diagnosis of the eccentricity fault and the composite fault are carried out. The average diagnostic accuracy and duration of the test set of these compared models are shown in Table 2.

Model 1 firstly extracted frequency features from the fault data and the model was trained only according to main harmonic amplitude. Due to the lack of other component features and the inevitability of the loss of effective features, the diagnosis accuracy of both types of fault is inferior despite the fact that the duration is shorter. The training process of model 2 is the same as the algorithm proposed in this paper. PSO without improvement was also used to determine the optimal DBN structure. However, the training accuracy and speed are worse than the algorithm proposed in this paper. Model 3 and 4 adopted a deep learning algorithm similar to the DBN and trained directly according to the original fault data, which can avoid the disadvantages of extracting frequency features through

signal processing technologies. Unfortunately, the structural parameters of SDAE, LSTM, and SVM were not optimized by any algorithms, which may lead to inaccurate feature extraction due to the improper number of nodes. Compared with the algorithm proposed in this paper, these two models are less accurate and require more time. Since the total sampled data of the composite fault is less than the counterpart of the single eccentricity fault, the average duration of the five models in the composite fault training and diagnosis is less than that of the single eccentricity fault. Except for the fact that the accuracy of model 1 decreases significantly, the diagnostic accuracy of other models is almost not affected. This also reflects that the deep learning model has strong generalization ability. In conclusion, EnFWA-DBN-ELM has obvious advantages in feature extraction and diagnosis of both the single eccentricity fault and the composite fault.

Table 2. Comparison of different diagnostic methods.

Algorithm	Single Eccentricity Fault		Composite Fault	
	Accuracy/%	Duration/s	Accuracy/%	Duration/s
FFT + EnFWA + DBN	89.882	8.46	86.718	6.19
PSO + DBN	95.622	11.04	94.371	9.88
SDAE + SVM	92.677	20.81	92.445	18.27
LSTM + Softmax	93.493	12.06	93.986	10.62
Algorithm of this paper	99.144	9.34	97.857	7.08

4. Data Collection and Diagnosis

In this section, the fault diagnosis adopts EnFWA algorithm to train the DBN-ELM model according to the fault data. Then, the fault diagnosis is carried out on the test data and the diagnosis accuracy is calculated later.

Deep learning networks mostly adopt the superimposed structure of three hidden layers, which can reduce the data reconstruction error. In this paper, four hidden layers with a $[X-H_1-H_2-H_3-H_4-T]$ structure which consists of three layers of RBM and a single layer of ELM are selected for the DBN. Moreover, iteration of the RBM for each layer is set as 20 with an initial momentum of 0.9 and a learning rate of 0.01. EnFWA is trained by 175 sets of preprocessed data to determine the optimal number of nodes in each hidden layer of the DBN-ELM network primarily and the range of nodes is [1, 500]. During training, the optimization was carried out iteratively according to the fitness of the average reconstruction error of all fireworks and its descendants in each iteration. The iteration ends when the fitness value $L_{fit} < 0.01$ or the number of iterations reaches 200. The fitness function L_{fit} is expressed as Equation (26):

$$L_{fit} = \frac{\sum_{i=1}^I \sum_{j=1}^J (p_{ij} - k_{ij})^2}{n^2} \quad (26)$$

In the formula, I is the number of RBM layers. J is the number of nodes in the hidden layer. n is the total number of fireworks and its descendants. p_{ij} is the reconstruction value of nodes. k_{ij} is the state of nodes.

There are seven fault categories to be studied. The original data of the output voltage and current at rated load of the aviation generator are collected by simulation, as shown in Table 3. Setting the sampling rate to 50 kHz and the single sampling time to 0.1 s. The six sampled data are mixed into a group with a total of 30,000 sample points, collecting 30 groups of data for each fault with a total of 210 groups. Finally, a $210 \times 30,000$ original dataset is obtained.

After noise preprocessing and normalization of the original data, 210 groups of fault data which consist of 30 groups for each of the seven fault categories are obtained and 25 groups of each category are selected as the training set from 30 groups of each category. Then, another five groups of each category are used as the test set. The optimal DBN model is obtained by the EnFWA based on 175 groups of the fault data of the aviation

generator. While the remaining 35 groups of the test data are diagnosed and the diagnostic accuracy was calculated. At the beginning of the training, the RBM error determined by each firework is large. With the increase in iteration and the continuous updating of fireworks generation, RBM parameters are gradually optimized and the training error decreases accordingly. The fitness curve is shown in Figure 19. According to the curve, after 140 training, the minimum error is 0.00855, which meets the end condition of the iteration. Meanwhile, the number of nodes of the four hidden layers is determined to be [114, 298, 396, 403].

Table 3. Collected data and fault labels.

Fault Category	Type	Training Data	Test Data
1	Normal	7.5×10^5	1.5×10^5
2	1/9 A phase short-out + 5% Dynamic eccentricity	7.5×10^5	1.5×10^5
3	1/9 A phase short-out + 5% Static eccentricity	7.5×10^5	1.5×10^5
4	2/9 A phase short-out + 15% Dynamic eccentricity	7.5×10^5	1.5×10^5
5	2/9 A phase short-out + 15% Static eccentricity	7.5×10^5	1.5×10^5
6	3/9 A phase short-out + 25% Dynamic eccentricity	7.5×10^5	1.5×10^5
7	3/9 A phase short-out + 25% Static eccentricity	7.5×10^5	1.5×10^5

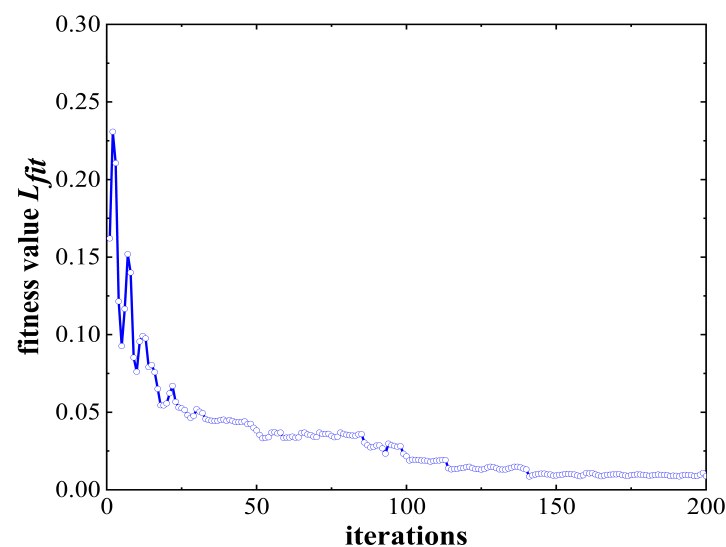


Figure 19. Fitness curve.

With this structure, the result of the training set is shown in Figure 20 and the diagnosis accuracy reaches 100%. Further, the diagnosis result of the test set with 97.1429% accuracy is shown in Figure 21. In these two figures, the Y-axis represents the category of the fault shown in Table 3 and the X-axis represents the serial number of the training set or the test set, where the training set contains 175 groups and the test set is 35. The diagnosis accuracy of the training set and test set are 97.6% and 97.857%, respectively, with 7.08 s average duration after 20 calculations. Compared with the single eccentricity fault diagnosis, the accuracy of the proposed method in this paper is reduced slightly under the circumstance of the composite fault. In addition to the reduction in the training sample, the main features of short-out among mixed features will affect the ability of the model to identify the secondary feature of eccentricity. In another way, the feature of eccentricity is less obvious than the short-out. Sample No. 11 of the test set in Figure 21 has the same degree of short-out as other samples in the group, but the diagnosis result is wrong.

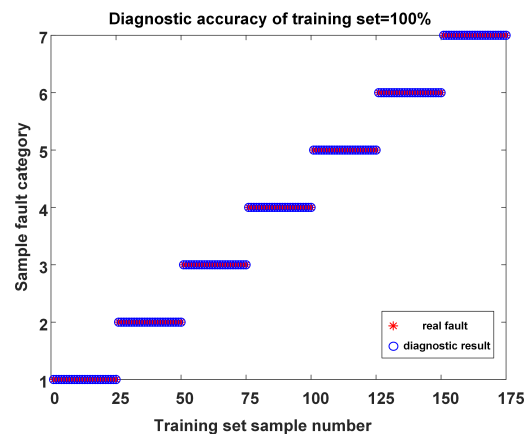


Figure 20. Diagnosis result of training set.

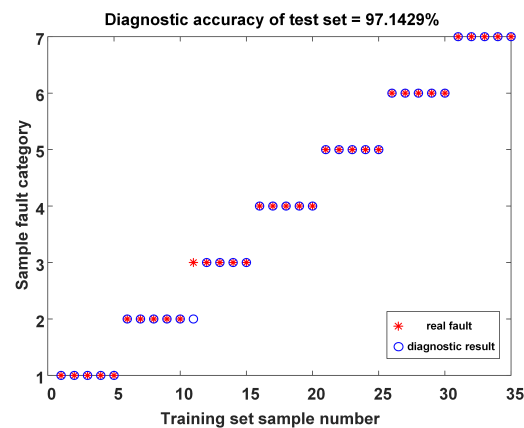


Figure 21. Diagnosis result of test set.

5. Conclusions

In this paper, the finite element simulation model of a 65kVA aviation generator is established and the fault model is set up for the short-out of stator windings, the static eccentricity, and the dynamic eccentricity. A fault diagnosis method based on EnFWA-DBN-ELM is proposed to realize the feature extraction and diagnosis of the composite faults of the aviation generator. This algorithm makes full use of the output voltage and current data of the aviation generator under the fault condition without additional signal processing. The optimization ability of the EnFWA is significantly improved and enables the fast and efficient optimization of DBN. Comparisons with other models are settled to validate the proposed model. The result of the comparisons shows that the proposed algorithm has an outstanding optimization ability that enables the model to diagnose the fault accurately and fast. Benefit from this, the fault diagnosis efficiency of the aviation generator can be improved. Furthermore, EnFWA-DBN-ELM is suitable for offline or online fault detection of the aviation generator as an effective auxiliary maintenance method.

Author Contributions: Conceptualization, Z.Y.; methodology, Z.Y.; software, X.B.; validation, Z.Y. and X.B.; formal analysis, Z.Y. and X.B.; investigation, X.B. and Q.Z.; resources, X.B.; data curation, X.B. and J.Y.; writing—original draft preparation, X.B. and Q.Z.; writing—review and editing, X.B. and J.Y.; visualization, X.B. and Q.Z.; supervision, X.B. and J.Y.; project administration, X.B. and J.Y. All authors have read and agreed to the published version of the manuscript.

Funding: This research was funded by National Natural Science Foundation of China, grant number 51407185, U1533126.

Data Availability Statement: Not applicable.

Conflicts of Interest: The authors declare no conflict of interest.

Abbreviations

The following abbreviations are used in this manuscript:

FWA	Fireworks Algorithm
EnFWA	Enhanced Fireworks Algorithm
ELM	Extreme Learning Machine
DBN	Deep Belief Network
DC	Direct Current
RBM	Restricted Boltzmann Machine
FFT	Fast Fourier Transform
PSO	Particle Swarm Optimization
FEM	Finite Element Method
BEF	Back Electromotive Force
RMS	Root Mean Square
SDAE	Stacked Denoising Auto Encoder
SVM	Support Vector Machine
LSTM	Long Short Term Memory

References

1. IEEE Std. IEEE Recommended Practice for the Design of Reliable Industrial and Commercial Power Systems—Redline. In *IEEE Std 493-2007 (Revision of IEEE Std 493-1997)—Redline*; IEEE: Piscataway, NJ, USA, 2007; pp. 1–426.
2. Sadeghi, I.; Ehya, H.; Faiz, J. Analytic method for eccentricity fault diagnosis in salient-pole synchronous generators. In Proceedings of the 2017 International Conference on Optimization of Electrical and Electronic Equipment (OPTIM) & 2017 Intl Aegean Conference on Electrical Machines and Power Electronics (ACEMP), Brasov, Romania, 25–27 May 2017; pp. 261–267. [\[CrossRef\]](#)
3. He, Y.L.; Zhang, W.; Xu, M.X.; Tao, W.Q.; Liu, H.L.; Dou, L.J.; Wan, S.T.; Li, J.Q.; Gerada, D. Rotor loss and temperature variation under single and combined faults composed of static air-gap eccentricity and rotor inter-turn short circuit in synchronous generators. *IET Electr. Power Appl.* **2021**, *15*, 1529–1546. [\[CrossRef\]](#)
4. Ehya, H.; Nysveen, A.; Nilssen, R.; Liu, Y. Static and dynamic eccentricity fault diagnosis of large salient pole synchronous generators by means of external magnetic field. *IET Electr. Power Appl.* **2021**, *15*, 890–902. [\[CrossRef\]](#)
5. Zhang, J.; Xiong, X.; Zhou, Y.; Wang, K. Rotor Eccentric Diagnosis of High-Voltage Motor in Nuclear CRF Pump Using Vibration Signals. In Proceedings of the 2021 7th International Conference on Condition Monitoring of Machinery in Non-Stationary Operations (CMMNO), Guangzhou, China, 11–13 June 2021; pp. 282–286. [\[CrossRef\]](#)
6. Shuting, W.; Yuling, H. Analysis on stator circulating current characteristics of turbo-generator under eccentric faults. In Proceedings of the 2009 IEEE 6th International Power Electronics and Motion Control Conference, Wuhan, China, 17–20 May 2009; pp. 2062–2067. [\[CrossRef\]](#)
7. Swana, E.F.; Doorsamy, W. Investigation of Combined Electrical Modalities for Fault Diagnosis on a Wound-Rotor Induction Generator. *IEEE Access* **2019**, *7*, 32333–32342. [\[CrossRef\]](#)
8. Tamilselvan, P.; Wang, P. Failure diagnosis using deep belief learning based health state classification. *Reliab. Eng. Syst. Saf.* **2013**, *115*, 124–135. [\[CrossRef\]](#)
9. Yang, L.; Wang, J.; Zhang, G.; Li, X.; Fu, H. An Adaptive Fault Diagnosis System Framework for Aircraft Based on Man-in-loop. In Proceedings of the 2019 IEEE International Conference on Prognostics and Health Management (ICPHM), San Francisco, CA, USA, 17–20 June 2019; pp. 1–4. [\[CrossRef\]](#)
10. Tran, V.T.; AlThobiani, F.; Ball, A. An approach to fault diagnosis of reciprocating compressor valves using Teager-Kaiser energy operator and deep belief networks. *Expert Syst. Appl.* **2014**, *41*, 4113–4122. [\[CrossRef\]](#)
11. Tran, V.T.; AlThobiani, F.; Tinga, T.; Ball, A.; Niu, G. Single and combined fault diagnosis of reciprocating compressor valves using a hybrid deep belief network. *Proc. Inst. Mech. Eng. Part C-J. Mech. Eng. Sci.* **2018**, *232*, 3767–3780. [\[CrossRef\]](#)
12. Luo, H.; He, C.; Zhou, J.; Zhang, L. Rolling Bearing Sub-Health Recognition via Extreme Learning Machine Based on Deep B Network Optimized by Improved Fireworks. *IEEE Access* **2021**, *9*, 42013–42026. [\[CrossRef\]](#)
13. Zheng, S.; Li, J.; Janecek, A.; Tan, Y. A Cooperative Framework for Fireworks Algorithm. *IEEE-ACM Trans. Comput. Biol. Bioinform.* **2017**, *14*, 27–41. [\[CrossRef\]](#) [\[PubMed\]](#)
14. Gohari, M.; Eydi, A.M. Modelling of shaft unbalance: Modelling a multi discs rotor using K-Nearest Neighbor and Decision Tree Algorithms. *Measurement* **2020**, *151*, 107253. [\[CrossRef\]](#)
15. Luo, S.; Cheng, J.; Zeng, M.; Yang, Y. An intelligent fault diagnosis model for rotating machinery based on multi-scale higher order singular spectrum analysis and GA-VPMCD. *Measurement* **2016**, *87*, 38–50. [\[CrossRef\]](#)
16. Shao, H.; Jiang, H.; Zhang, X.; Niu, M. Rolling bearing fault diagnosis using an optimization deep belief network. *Meas. Sci. Technol.* **2015**, *26*, 115002. [\[CrossRef\]](#)
17. Wu, S.; Zheng, L.; Hu, W.; Yu, R.; Liu, B. Improved Deep Belief Network and Model Interpretation Method for Power System Transient Stability Assessment. *J. Mod. Power Syst. Clean Energy* **2020**, *8*, 27–37. [\[CrossRef\]](#)

18. Shan, H.; Sun, Y.; Zhang, W.; Kudreyko, A.; Ren, L. Reliability Analysis of Power Distribution Network Based on PSO-DBN. *IEEE Access* **2020**, *8*, 224884–224894. [[CrossRef](#)]
19. Zhang, C.; He, Y.; Yuan, L.; Xiang, S. Analog Circuit Incipient Fault Diagnosis Method Using DBN Based Features Extraction. *IEEE Access* **2018**, *6*, 23053–23064. [[CrossRef](#)]
20. Mackerle, J. FEM and BEM analysis and modelling of residual stresses—A bibliography (1998–1999). *Finite Elem. Anal. Des.* **2001**, *37*, 253–262. [[CrossRef](#)]

Disclaimer/Publisher’s Note: The statements, opinions and data contained in all publications are solely those of the individual author(s) and contributor(s) and not of MDPI and/or the editor(s). MDPI and/or the editor(s) disclaim responsibility for any injury to people or property resulting from any ideas, methods, instructions or products referred to in the content.